Dynamic Analysis of Radial Electric Field and Plasma Temperature using Extended Transport Model

Tsukamoto, Asako
Interdisciplinary Graduate School of Engineering Sciences, Kyushu University

Ito, Sanae-I.
Research Institute for Applied Mechanics, Kyushu University

Yagi, Masatoshi
Research Institute for Applied Mechanics, Kyushu University

https://doi.org/10.15017/26797

出版情報：九州大学応用力学研究所所報. 129, pp.73-88, 2005-09. Research Institute for Applied Mechanics, Kyushu University

Dynamic Analysis of Radial Electric Field and Plasma Temperature using Extended Transport Model

Asasko TSUKAMOTO *1, Sanae -I. ITOH *2, Masatoshi YAGI*2,
E-mail of corresponding author: *asako@riam.kyushu-u.ac.jp*

(Received July 29, 2005)

Abstract

We have develpoed the extended transport model based on MHD ordering to incorporate not only non-ambipolar loss flux but also turbulent diffusivity due to ITG turbulence with $E \times B$ shearing rate . Using this model, we investigate the influence of fluctuation on transition and transport. The self-oscillation is observed when the perturbation is appled in the plasma boundary. To check the sensitivity of numerical scheme and transport model on the self-oscillation, we compare results of the different formula of $E \times B$ shearing rate and of the threshold function in the thermal diffusivity. The dependence of grid spacing in the numerical calculation is also investigated.

Key words : *ELM activity, L-H transition, ITG, EXB shearing rate, transport, MHD*

1. Introduction

To utilize the released energy from the controlled thermonuclear fusion is a candidate as a new energy source of the next generations. The necessary temperature for self-ignition is about 10keV. Since such high temperature precludes the confinement by the material walls, magnetic field is used to confine a plasma within a chamber without the contact with the wall. Tokamak device has been the most extensively investigated and advanced. In a tokamak reactor, it would be necessary to confine the energy of enough dense plasma for a time which allows an adequate fraction of the fuel to react.

The improved confinement regime known as H-mode is a candidate for advanced operation, however, it is often perturbed by the onset of a quasi-periodic series of relaxation oscillations involving bursts of MHD activity and D_α emission, named by edge localized modes (ELMs). These result in rapid losses of particles and energy from the region near the plasma boundary, reducing the average global energy confinement, although, the ELMs are more efficient, and beneficial, in removing density and impurities. Thus they are deemed necessary for the stationary H-mode operation of ITER. It is, therefore, desirable to be able to control the level and nature of the ELM activity.

A theory based on the bifurcation of the radial electric field E_r was proposed by Itohs and Shaing [1, 2]. This model is derived from the ambipolar condition due to a momentum source/sink or bipolar loss. The hard type bifurcation is predicted from the stationary condition. Later, it was extended by introducing spatio-temporal variation [3]. The extended model is similar to the time-dependent Ginzburg-Landau type equation. It has a hysteresis characteristics for the flux-gradient relation and shows the limit-cycle behavior which may be related with ELMs.

In these theories, L-H transition occurs when a set of plasma parameters reaches a certain critical condition. That is, it stands on a deterministic view. However, in reality, L-H transition takes place in low confinement mode (L-mode) state where the confinement is dominated by microturbulence. Therefore, it is natural to introduce statistical variances in relevant variables, and the transition is modelled as turbulence-turbulence transition [4]. In Ref. [5], the probabilistic nature of the transition is investigated using 0-D model. Our aim of this research is to develop transition model including turbulence fluctuation and to investigate the influence of fluctuation for transition and transport.

The organization of this thesis is as follows. In Chapter 2, we review L-H transition models, the model of ELM activity as a limit cycle, and the probabilistic model of L-H transition. In Chapter 3, an extended transport model which describes the time evolution of ion temperature and radial electric field is derived from the reduced MHD model. The numerical analysis is per-

*1 Interdisciplinary Graduate School of Engineering Sciences, Kyushu University
*2 Research Institute for Applied Mechanics, Kyushu University

formed using this model. The self-oscillation is observed when the perturbation is applied in the plasma boundary. To check the sensitivity of numerical scheme and transport model on the self-oscillation, we compare results using the different formula of E×B shearing rate and of the threshold function in the thermal diffusivity χ. The dependence of grid spacing in the numerical calculation is also investigated. Finally, summary and discussions are given in Chapter 4.

2. Reviews

The improved confinement regime known as H-mode is often perturbed by the onset of a quasi-periodic series of relaxation oscillations involving bursts of MHD activity and D_α emission, known as ELMs. Two types of local model for the L-H transition have been proposed. One is based on the non-ambipolar losses such as ion loss-cone loss, ion poloidal viscous damping, the other is based on the interaction between the turbulence and zonal flow through the reduction of anomalous transport due to the radial electric field shear. By taking spatio-temporal variation into account, the limit-cycle behavior resembling ELMs is reproduced by these models.

2.1 Local L-H Transition Model

The L-H transition theory based on the bifurcation of the radial electric field E_r, which is determined by the non-ambipolar loss flux was firstly proposed by Itohs [1]. A bifurcation in the particle flux associated with the change of the radial electric field is found, which implies that the particle and energy fluxes can have multiple values for the same density and temperature values. The threshold power for the transition was predicted by this theory. The ion flux in the region of $|a-r| \leq \rho_{pi}$ is attributed to the direct orbital loss (a: minor radius, $\rho_{pi} \equiv v_{T_i}/\Omega_{cp}$, $\Omega_{cp} = \frac{eB_p}{m_i}$, B_p; poloidal magnetic field, other notations are conventional ones.).

The ion orbital loss was given by

$$\Gamma_i = (n_i \nu_{ii}/\sqrt{\epsilon})\rho_{pi} F, \tag{1}$$

where the coefficient F is proportional to the relative number of particles in the loss cone in the velocity space, $0 < F < 1$, and n_i is the ion density. ϵ is the inverse aspect ratio of the torus ($\epsilon = a/R$). In order to estimate F in the presence of E_r, two simple assumptions were made. (1) The ions which satisfy the resonance condition $v_\parallel/qR = E_r/rB_t$ (or, $v_\parallel = E_r/B_p$.) are lost directly. B_t is toroidal magnetic field. (2) The ion distribution function f_i is close to the Maxwellian, $f_i \propto \exp(-v_\parallel^2/v_{Ti}^2)$. Then the estimation $f_i \propto \exp\{-(\rho_{pi} e E_r/T_i)^2\}$ was made and the ion loss has the form;

$$\Gamma_i^{lc} = \frac{n_i \nu_{ii} \rho_{pi} \hat{F}}{\sqrt{\epsilon}} \exp\left\{ -\left(\frac{e\rho_{pi}E_r}{T_i}\right)^2 \right\}, \tag{2}$$

where the coefficient $\hat{F}$ is the contribution of the bounce average. On the other hand, the electron loss was taken as

$$\Gamma_e^{anom} = -D_e n_e \left(\frac{n_e'}{n_e} + \alpha_1 \frac{T_e'}{T_e} + \frac{eE_r}{T_e} \right), \tag{3}$$

where α_1 is a numerical coefficient of the order of unity. D_e is the anomalous electron diffusivity. Equating Eqs.(1) and (2), the equation to determine the ambipolar electric field was given by

$$\exp\left\{ -\left(\frac{e\rho_{pi}E_r}{T_i}\right)^2 \right\} = d_1 \left\{ \lambda - \left(\frac{e\rho_{pi}E_r}{T_i}\right) \right\} (\equiv \hat{\Gamma}), \tag{4}$$

where $d_1 = D_e\sqrt{\epsilon}/(\rho_{pi}^2 \hat{F} \nu_{ii})$ and $\lambda = -\rho_{pi}(T_e/T_i)(n_e'/n_e + \alpha_1 T_e'/T_e)$. Fig. 1(a) illustrates the λ dependence of $\hat{\Gamma}$ as the solution of Eq.(4). When λ is below the critical value λ_c, the electric field turns to positive and the fluxes are reduced. The L-mode corresponds to the branch of the large loss flux and the H-mode is the reduced loss flux. Fig. 1 illustrates the bifurcation from the L- to H-mode take place as $A \to B' \to C \to C' \to D$ and that from the H- to L-mode occurs at $D \to C' \to B \to B' \to A$. Because λ_c for the L- to H-mode transition is larger than that for the H- to L-mode transition, there is a hysteresis in the relation of $\hat{\Gamma}$ and λ as is shown in Fig. 1(a).

An extended model for the L-H transition was reported in Ref. [2]. The poloidal flow velocity U_p was chosen as an independent variable instead of E_r. To determine U_p, the poloidal momentum equation was solved. In standard neoclassical theory, the poloidal momentum is damped by the poloidal (parallel) viscosity $< \mathbf{B_p} \cdot \nabla \cdot \overleftrightarrow{\pi} >$, because there is neither a momentum source nor a sink. Here $\overleftrightarrow{\pi}$ is the ion viscosity tensor and the angular bracket denotes the flux surface average. In the edge region, the poloidal rotation is driven by the torque or viscosity associated with the ion orbit loss or any other radial currents. The quantity $< \mathbf{B_p} \cdot \nabla \cdot \overleftrightarrow{\pi} >$ was calculated by solving the drift kinetic equation with mass flow velocity. The result is

$$< \mathbf{B}_p \cdot \nabla \cdot \overleftrightarrow{\pi} > = \frac{\sqrt{\pi}}{4} \frac{\epsilon^2}{r} n_i m_i v_{Ti} B_t \left(I_p U_p + I_T U_{p0} \right), \tag{5}$$

where $U_{p0} = -\rho_i (dT_i/dr)/T_i$, n_i is the plasma density and ρ_i is the ion gyroradius. The integrals I_p and I_T are defined as

$$\left\{ \begin{array}{c} I_p \\ I_T \end{array} \right\} = \frac{1}{\pi} \int_0^{\sqrt{\nu_{*i}}} dx \left\{ \begin{array}{c} 1 \\ (\frac{5}{2} - x) \end{array} \right\} x^2 \exp(-x^2)$$
$$\times \int_{-1}^{1} d\left(\frac{v_\parallel}{v}\right) \left| 1 - 3\left(\frac{v_\parallel}{v}\right)^2 \right|^2$$

$$\times \frac{\nu_{*i}\epsilon^{3/2}\left(\nu_T/(\nu_{ii}\sqrt{x})\right)}{\left(v_{\|}/v + U_{p,m}/\sqrt{x}\right)^2 + \left|\ \nu_{*i}\epsilon^{3/2}\left(\nu_T/(\nu_{ii}\sqrt{x})\right)\ \right|^2}, \quad (6)$$

where $U_{p,m} = U_p B/(v_{Ti}B_p) + \lambda_p/2$, $\lambda_p = -\rho_{pi}(dp/dr)/p$, $\nu_{*i} = \nu_{ii}Rq/(v_{Ti}\epsilon^{3/2})$ and ν_T is the collision frequency for the anisotropy relaxation. The ion orbit loss rate was estimated to be

$$\left(\frac{\partial n_i}{\partial t}\right)_{orbit} = -\frac{n_i\nu_{ii}G}{\left\{\nu_{*i} + \left(\alpha U_{p,m}\right)^4\right\}^{1/2}} \times \exp\left\{-\left|\ \nu_{*i} + \left(\alpha U_{p,m}\right)^4\ \right|^{1/2}\right\}, \quad (7)$$

where G is a geometric factor of the order of unity that depends on the detailed shape of the loss cone in phase space and α, a numerical constant, accounts for the orbit shape, such as orbit squeezing.

The particle flux associated with ion orbit loss was estimated to be

$$\Gamma_i^{lc} = \frac{Gn_i\nu_{ii}\triangle r}{\left\{\nu_{*i} + \left(\alpha U_{p,m}\right)^4\right\}^{1/2}} \times \exp\left\{-\left|\ \nu_{*i} + \left(\alpha U_{p,m}\right)^4\ \right|^{1/2}\right\}, \quad (8)$$

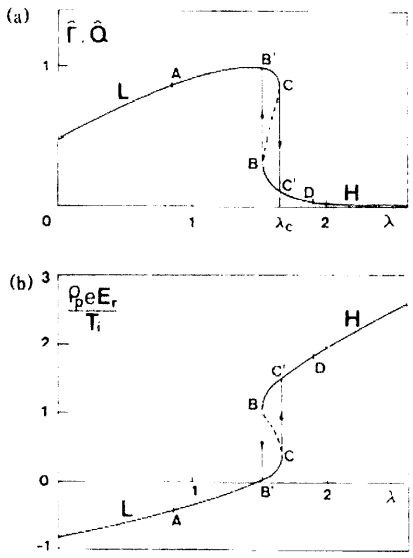

Fig. 1 Solutions for (a) the normalized flux and (b) the radial electric field a function of λ (for the case of $d_0 = 1.3$). Transition from the branch of the large flux to that of small flux occurs as $\lambda = \lambda_c$. (cited from Ref. [1])

where $\Gamma_i^{lc} = -\vec{r}(\triangle r)(\frac{\partial n_i}{\partial t})_{orbit}$, $\triangle r$ is the characteristic width over which the ion orbit loss is important, $\vec{r}$ is the unit vector. Equation (8) gives an extended form of Eq.(2). The poloidal momentum balance equation leads

$$-(e/c)\mathbf{\Gamma_i^{lc}} \times \mathbf{B} \cdot \mathbf{B_p} = < \mathbf{B_p} \cdot \nabla \cdot \overleftrightarrow{\pi} > . \quad (9)$$

Substituting Eqs.(5) and (8) into Eq.(9), an algebraic equation for U_p was given as

$$\frac{\nu_{*i}G}{\left\{\nu_{*i} + \left(\alpha U_{p,m}\right)^4\right\}^{1/2}} \exp\left\{-\left|\ \nu_{*i} + \left(\alpha U_{p,m}\right)^4\ \right|^{1/2}\right\} = -\frac{\sqrt{\pi}}{4}\left(\frac{\sqrt{\epsilon}\rho_{pi}}{\triangle r}\right)\left(I_p\frac{U_pB_t}{v_{Ti}B_p} + \frac{I_tU_{p0}}{v_{Ti}}\frac{B_t}{B_p}\right). \quad (10)$$

The solution of Eq.(10) was obtained graphically by examining the intersections of two functions, $Y_1(U_{p,m})$ [the left side of Eq.(10)] and $Y_2(u_{p,m})$ [the right side of Eq.(10)] for a given set of parameters. As an example, parameters were set as followed: $G = 1$, $(\pi\epsilon)^{1/2}\rho_{pi}/(4\triangle r) = 1.36$, $\epsilon = 0.25$, $\alpha = 0.5$, for simplicity, $\lambda_p = 0.2$ and $U_{p0}B/(v_{Ti}B_p) = 0.2$. ν_{*i} was chosen as the control parameter. As can be seen from Fig. 2, at $\nu_{*i} = 2.0$, there are three solutions of U_p. Two solutions are stable and the one in the middle is unstable. The solution close to the origin is the continuation of the L root; the more negative stable solution is the new root (H root), which does not exist if there is no ion orbit loss. When ν_{*i} decreases further more, negative H root exists. $U_{p,m}$ is the function of ν_{*i} for the same parameters as in Fig. 2. The critical ν_{*i} at which E_r makes a sudden change to be more negative was either greater than or less than unity.

2.2 Time-dependent L-H Transition Model

By taking account of spatio-temporal variation in the 0-dimensional L-H transition model, the limit-cycle behavior resembling ELMs can be obtained. It has been extended to the diffusive type transport equations [6]. The one dimensional transport equations for normalized density n and radial electric field Z, are given by

$$\frac{\partial n}{\partial t} = \frac{\partial}{\partial x}D(z)\frac{\partial n}{\partial x}, \quad (11)$$

$$\epsilon\frac{\partial Z}{\partial t} = -N(Z,g) + \mu\frac{\partial^2 Z}{\partial x^2}, \quad (12)$$

where

$$Z = e\rho_{pi}E_r/T_i, \quad (13)$$

and ϵ denotes the dynamical time difference between n and γ (v_A : Alfvén velocity and c: light speed);

$$\epsilon = (1 + v_A^2/c^2)B_p^2/B^2 \simeq B_p^2/B^2, \quad (14)$$

and ion shear viscosity μ and effective loss D are comparable in magnitude. N is the nonlinear function of

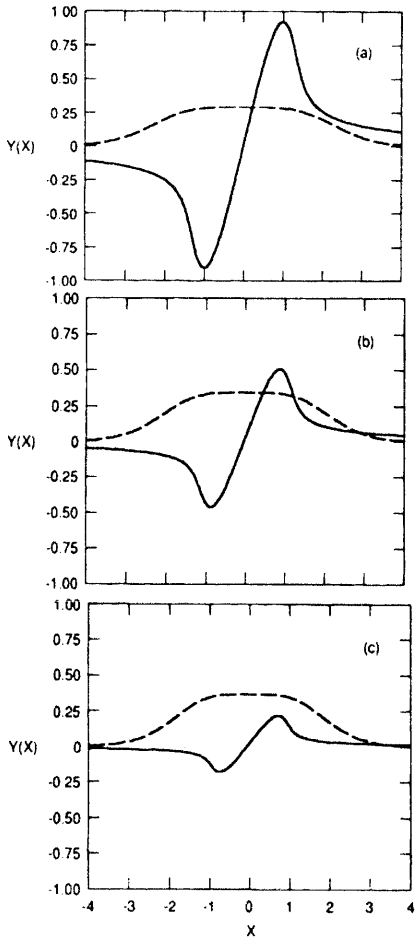

Fig. 2 The transition of $U_{p,m} \equiv X$ from (a) the L root to (b) the multiple-root state an finally to (c) the H root as ν_{*i} decreases. The dashed lines are $Y_1(X)$, and the solid lines are $Y_1(X)$ (cited from Ref [2]).

the radial electric field Z and the non-ambipolar flux g given by

$$g = d\lambda = -\frac{\rho_{pi}}{\nu_{*i}}\frac{n'}{n}, \tag{15}$$

where $\lambda = \rho_{pi}/L_n$, $d = D_0/\nu_{ii}\rho_{pi}^2$. ρ_{pi} is a poloidal ion Larmor radius, L_n, density scale length and D_0, typical electron diffusivity. D is assumed to be a smooth function of Z;

$$D(Z) = \frac{D_{min} + D_{max}}{2} + \frac{D_{max} - D_{min}}{2}\tanh Z. \tag{16}$$

In addition, a model S-curve for N is assumed as

$$N(z, g) = g - g_0 + \beta Z^3 - \alpha Z. \tag{17}$$

$N(Z, g) = 0$ gives multiple solutions in particular conditions as is shown by the local theory (Fig. 3).

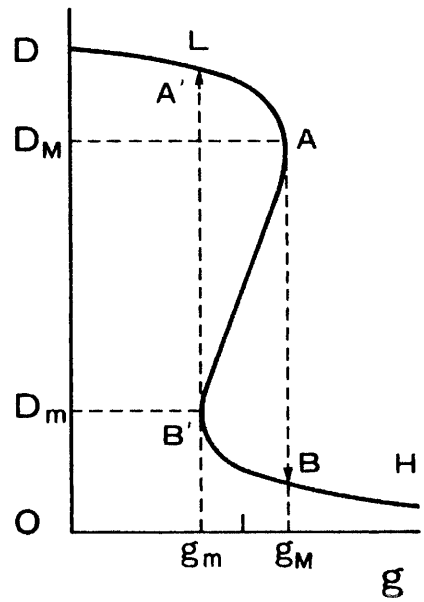

Fig. 3 A model of effective diffusivity D i.e. the ratio of the particle flux to the density gradient as a function of gradient parameter g from Ref. [6], showing the possibility of bifurcations and hysteresis.

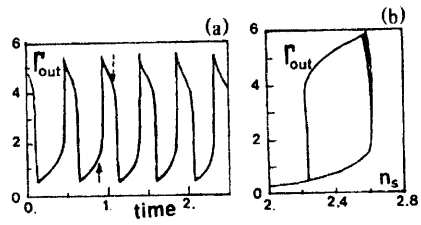

Fig. 4 (a) Temporal evolution of the outflux Γ_{out} corresponding to the model in Fig. 3 (b) Lyssajous figure for the edge density and the outflux.

The boundary condition is given by

$$-\frac{n'}{n}_{x=0} = const. \tag{18}$$

$$\Gamma = \Gamma_{in,x=-L} \tag{19}$$

Periodic solutions for edge density and loss flux Γ_{out} are found in the restricted parameter range near the L-H transition condition. The behavior of Γ_{out} resembles the D_α emission during ELMs. The parameter space for these limit cycles is given by

$$D_m/g_m < \Gamma_{in}\lambda_s^2 < D_M/g_M, \tag{20}$$

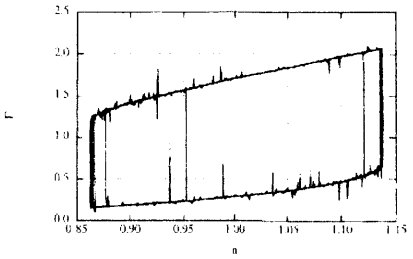

Fig. 5 The Lyssajous figure n and $\Gamma = \gamma n$ for the case of power noises.

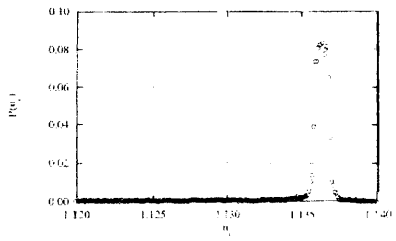

Fig. 6 Distribution of the critical density at the onset of the transition for the noise with power law. Statistical distribution of critical density is obtained.

where $\lambda_s \equiv n/n'$ is evaluated at the edge, and

$$g_{m,M} = g_0 \mp 2\beta(\alpha/3\beta)^{3/2}, \tag{21}$$

$$D_{m,M} = D(Z = \pm\sqrt{\alpha/3\beta}). \tag{22}$$

2.3 Probabilistic L-H Transition Model

The probabilistic nature of the transition by using the 0-D dynamical model is investigated in Ref. [5]. This model is the simplified version of 1-D model, which includes the hysteresis characteristic [3]. This model consists of temporal evolution of the density and the loss rate which produces the hysteresis of the flux-density relation. The mean density n and the loss rate γ are taken as the representative variables. The loss rate is directly related to the turbulence level and the particle diffusivity. A layer with a finite width is considered, and the averaged value within this layer is treated as a scalar quantity. This is the simplified model of the hysteresis, however, it has successfully applied to the investigation of the dynamics of dithering ELMs. The model equation takes the form

$$\frac{\partial}{\partial t} n = S - \gamma n, \tag{23}$$

and

$$\epsilon \frac{\partial}{\partial t} \gamma = n - 1 + a(\gamma - 1) - b(\gamma - 1)^3, \tag{24}$$

where S is the particle influx into layer, and the cubic equation $a(\gamma - 1) - b(\gamma - 1)^3$ describes the shape of the hysteresis in the typical value for the L-mode. If all the coefficients (S, a, b, γ) are constant in time, Eqs.(23) and (24) predict the stable stationary solutions or the dynamical solution of a limit cycle. Stationary solutions are obtained for $S < S_1$ (lower flux blanch), $S_2 < S$ (higher flux blanch), and limit cycle appears for $S_1 < S < S_2$, where $S_1 = (1 - \sqrt{a/3b})\{1 + (2a/3)\sqrt{a/3b}\}$ and $S_2 = (1 + \sqrt{a/3b})\{1 - (2a/3)\sqrt{a/3b}\}$. The transition from H-mode to L-mode takes place at $n_{c0} = 1 + (2a/3)\sqrt{a/(3b)}$, i.e., n_{c0} is the threshold condition in the absence of noises. If the parameters are chosen as $a = 0.5$ and $b = 1.0$, the critical fluxes are given by $S_1 = 0.67$ and $S_2 = 1.21$. When $S = 0.6$ for the other fixed parameters, no oscillation appears. We set $S = S_0 + \delta_s$. Without a statistical deviation from the average, there are a clear boundary at $S_0 = S_1$; no limit cycle is excited in the region $S_0 < S_1$. When the noise in the source ϵ_a, which obeys the power law ,i.e., probabilistic function $P(\delta_s) \propto |\delta_s|^{-2}$, the oscillation like limit cycles with irregular bursts are obtained. The Lyssajous figure of n v.s. $\Gamma(= \gamma n)$ is shown in Fig. 5. The distribution of the critical density at the onset of transition, $P(n_c)$, is obtained in Fig. 6. The value of n_c which takes the maximum probability nearly equals to n_{c0}, where the transition occurs in the absence of noise. The distribution clearly demonstrates that the onset has a probabilistic nature.

3. Dynamic Analysis of Radial Electric Field and Temperature

We derive an extended transport model based on the three-field reduced MHD equation. Our extended transport model is new and consists of the time evolution of ion temperature and poloidal flow. For simplicity, we assume $T_e = T_{e0}$, and ignore the fluctuation of electron. Thermal diffusivity driven by ion temperature gradient (ITG) driven drift wave turbulence is expressed as the function of ion temperature and poloidal flow such as $\chi^{ITG} = \chi^{ITG}(U_p, T_i) = (\gamma^{ITG}/k_\perp^2)(1-\Omega^2)$, where χ^{ITG} proposed by F.Romanelli [8], and the E×B shearing rate Ω proposed by P. H. Diamond et.al. [11] are adoppted in this thesis.

3.1 Model Equation

According to the transport ordering ($\rho_i/\ell = \omega/\Omega_i \ll 1$, ρ_i; ion Larmor radius, ℓ; system size, ω; characteristic frequency, Ω_i; ion cyclotron frequency), the time

evolution of radial electric field is given by [3)]

$$\left(1+\frac{c^2}{v_A^2}\right)\epsilon_0\frac{dE_r}{dt}=-e\Big(\Gamma_i-\Gamma_e\Big)+\frac{e\rho_p n_i}{B_p v_{Ti}}\mu_i\frac{\partial^2}{\partial x^2}E_r, \tag{25}$$

where the non-ambipolar ion and electron fluxes are given by

$$\Gamma_i=\frac{n_i\nu_{ii}\rho_p}{\sqrt{\epsilon}}e^{-Z^2}, \tag{26}$$

and

$$\Gamma_e=-D_e n_e\left(\frac{n_e'}{n_e}+\alpha_1\frac{T_e'}{T_e}+\frac{eE_r}{T_e}\right), \tag{27}$$

with

$$Z=\frac{eE_r\rho_p}{T_i}. \tag{28}$$

ϵ_0 is the dielectric constant of vacuum. Introducing normalized variables;

$$d\equiv\frac{D_e\sqrt{\epsilon}}{\rho_p^2\nu_{ii}}\frac{T_i}{T_e}, \tag{29}$$

and

$$\lambda=-\rho_p\frac{T_e}{T_i}\left(\frac{n_e'}{n_e}+\alpha_1\frac{T_e'}{T_e}\right), \tag{30}$$

and keeping the dominant term in right hand side (RHS), we obtain

$$\epsilon\frac{\partial Z}{\partial\tau}=-\frac{1}{d}\frac{T_i}{T_e}\frac{D_e}{D_0}(e^{-Z^2}-d(\lambda-Z))+\hat{\mu}\frac{\partial^2 Z}{\partial y^2}, \tag{31}$$

where $\hat{\mu}=\mu_i/D_0$. Normalization has been done as $tD_0/\rho_p^2\to\tau$, $x/\rho_p\to y$. This model was used to analyse L-H transition.

Next, we derive the model equation based on the three-field reduced MHD equations to include not only non-ambipolar flux as a source/sink but also turbulence effect, based on flute ordering($k_\parallel\sim O(\epsilon k_{bot})$, ϵ; a small parameter, $k_\parallel$; parallel wave number, $k_\perp$; perpendicular wave number). The vorticity equation is described as

$$\begin{aligned}&n_0m_i\left(\frac{\partial}{\partial t}\nabla_\perp^2F+[F,\nabla_\perp^2F]\right)-\frac{1}{\Omega_i}\nabla_\perp\cdot[p_i,\nabla_\perp F]\\&=\frac{B_o}{c}\nabla_\parallel(en_0v_\parallel)+en_0\frac{B_0}{c}\nabla F\times\nabla\Omega\cdot\hat{\mathbf{z}}\\&+\mu\nabla_\perp^4F+\frac{B_0}{c}\frac{d}{dr}J^r,\end{aligned} \tag{32}$$

where

$$F=\frac{c}{B_0}\left(\phi+\frac{1}{en_0}\tilde{p}_i\right) \tag{33}$$

is the generalized potential and

$$\tilde{p}_i=n_0\tilde{T}_i+\frac{en_0}{T_{e0}}T_{i0}\tilde{\phi}. \tag{34}$$

The ion parallel momentum equation is written by

$$n_0m_i\left(\frac{\partial}{\partial t}v_\parallel+\frac{c}{B_0}[\phi,v_\parallel]\right)=-en_0\nabla_\parallel F+4\mu\nabla_\perp^2v_\parallel. \tag{35}$$

The time evolution of ion temperature equation is given by

$$\begin{aligned}&\frac{3}{2}\left(\frac{\partial T_i}{\partial t}+\frac{c}{B_0}[\phi,T_i]\right)-T_{i0}\left(\frac{\partial n}{\partial t}+\frac{c}{B_0}[\phi,n]\right)\\&=-\nabla_\parallel q_\parallel+\kappa_\perp\nabla_\perp^2T_i+S,\end{aligned} \tag{36}$$

where

$$\frac{\partial n}{\partial t}+\frac{c}{B_0}[\phi,n]=\frac{\partial}{\partial t}\frac{en_0\phi}{T_{e0}}+\frac{d\phi_0}{dr}\frac{\partial n}{\partial\theta}-\frac{1}{r}\frac{\partial\phi}{\partial\theta}\frac{dn_0}{dr}. \tag{37}$$

For simplicity, the ion parallel momentum equation is neglected in the following processure, although it is straitforward to include it. Taking flux-surface average of Eq.(32) and neglecting the nonlinear term in LHS and once integrating it, we obtain

$$n_0m_i\frac{\partial}{\partial t}\frac{d}{dr}<F>=\mu\frac{d^3}{dr^3}<F>+\frac{B_0}{c}<J^r>, \tag{38}$$

This equation corresponds to Eq.(31) if we write $E_r*=-(B_0/c)dF/dr$. Similarly, we obtain

$$\frac{3}{2}n_0\frac{\partial}{\partial t}<T_i>=\kappa_\perp\frac{d^2}{dr^2}<T_i>+<S>. \tag{39}$$

where we neglect the perturbed part of n_0 since ITG does not produce a particle flux.

To evaluate J_r, Shaing's model [2)] is used;

$$J^r=e(\Gamma^{bv}+\Gamma^{lc}). \tag{40}$$

Γ^{bv} represents bulk viscosity;

$$\Gamma^{bv}=\frac{\sqrt{\pi}n_i\epsilon^2}{4r}\rho_{pi}\left(I_p\frac{U_pB}{v_{Ti}B_p}+I_t\frac{U_{p0}B}{v_{Ti}B_p}\right)v_{Ti}\frac{B_p}{B}. \tag{41}$$

U_{p0} is given by

$$U_{p0}=-\frac{\rho_iv_{Ti}}{2}\frac{1}{T_i}\frac{dT_i}{dr}=-\frac{1}{a}\frac{1}{\Omega_i}\frac{e}{m_i}\frac{1}{e}\frac{\partial T_i}{\partial\hat{r}}, \tag{42}$$

where $e/m_i=9.58\times10^7$, temperature is measured in $[eV]$, $\Omega_i=9.58\times10^7B$, and magnetic field is in $[T]$. $\hat{r}$ indicates the normalized radial variable by the minor radius; r/a. Γ^{lc} indicates the nonlinear ion orbit loss;

$$\Gamma^{lc}=\frac{n_i\nu_{ii}\triangle r}{(\nu_{*i}+(\alpha U_{p,m})^4)^{1/2}}\exp(-(\nu_{*i}+(\alpha U_{p,m})^4)^{1/2}), \tag{43}$$

where $\triangle r\sim\sqrt{\epsilon}\rho_{pi}$.

$$\begin{aligned}U_{p,m}&\equiv\frac{B}{v_{Ti}B_p}\frac{c}{B}\frac{\partial\phi}{\partial r}\\&=\frac{B}{v_{Ti}B_p}\left(U_p-\frac{1}{a}\frac{1}{\Omega_i}\frac{e}{m_i}\left(\frac{T_i}{e}\frac{1}{n}\frac{dn}{d\hat{r}}+\frac{1}{e}\frac{\partial T_i}{\partial\hat{r}}\right)\right).\end{aligned} \tag{44}$$

Then the extended transport equations are given by

$$\begin{aligned}\frac{\partial}{\partial t}U_p&=\frac{B_0}{cn_im_i}J^r\big(U_p,\nu_*(T_i)\big)\\&+\chi^{ITG}\frac{\partial^2}{\partial r^2}U_p+\chi_c\frac{\partial^2}{\partial r^2}U_p,\end{aligned} \tag{45}$$

$$\frac{3}{2}\frac{\partial}{\partial t}T_i = \chi^{ITG}\frac{\partial^2}{\partial r^2}T_i + S + \chi_c\frac{\partial^2}{\partial r^2}T_i + \chi^{NC}\frac{\partial^2}{\partial r^2}T_i. \quad (46)$$

χ^{ITG} is thermal diffusivity due to ITG turbulence including the E×B shearing rate;

$$\chi^{ITG} = \chi^{ITG}(U_p, T_i) = \frac{\gamma^{ITG}}{k_\perp^2}(1-\Omega^2). \quad (47)$$

The growth rate of ITG mode is given by

$$\gamma^{ITG} = \frac{k_y\rho_i v_{Ti}}{L_n}\epsilon_n^{1/2}\sqrt{\eta_i - \eta_{ic}}, \quad (48)$$

where $\epsilon_n = L_n/R_0$, $\eta_i = L_n/L_T$, $L_n = -1/(dlnn/dr)$ and $L_T = -1/(dlnT/dr)$. The wavenumber which gives the maximum growth rate is assumed to be $k_\perp\rho_i = 0.2$. According to Ref. [8], the threshold value for ITG is evaluated as

$$\eta_{ic} = \begin{cases} 1 & (\epsilon_n < 0.2) \\ 1 + 2.5(\epsilon_n - 0.2) & (\epsilon_n > 0.2) \end{cases} \quad (49)$$

The E×B shearing rate is given by

$$\Omega = \frac{k_\theta V'_{E\times B} W_K}{\gamma^{ITG}}, \quad (50)$$

where W_k is the mode width, and we assume

$$W_k \sim \frac{1}{k_\perp} \sim 5\rho_i. \quad (51)$$

χ^{NC} is the neoclassical diffusion coefficient and the interpolation formula is used;

$$\chi^{NC} = \frac{\epsilon^{1/2}\rho_{pi}^2}{\tau_i}\mathrm{K}_2^{(o)} \times\left(\frac{1}{1 + a_2\nu_{*i}^{1/2} + b_2\nu_{*i}} + \frac{\epsilon^{3/2}(c_2^2/b_2)\nu_{*i}\epsilon^{3/2}}{1 + c_2\nu_{*i}\epsilon^{3/2}}\right), \quad (52)$$

where $\mathrm{K}_2^{(o)} = 0.66$, $a_2 = 1.03$, $b_2 = 0.31$, $c_2 = 0.74$ [7]. Using the normalization:

$$r/a \to \hat{r}, v_{T_{io}}/at \to \hat{t}, \chi/(av_{T_{io}}) \to \hat{\chi}$$
$$Sa/(v_{T_{io}}) \to \hat{S}, \quad (53)$$

and $v^{bv} = \frac{\Gamma^{bv}}{n_i}$, $v^{lc} = \frac{\Gamma^{lc}}{n_i}$. we finally obtain the following transport equations:

$$\frac{\partial}{\partial \hat{t}}U_p = \frac{a}{\rho_{io}}\left(v^{bv} + v^{lc}\right) + \hat{\chi}^{ITG}\frac{\partial^2}{\partial \hat{r}^2}U_p + \hat{\chi}_c\frac{\partial^2}{\partial \hat{r}^2}U_p, \quad (54)$$

$$\frac{3}{2}\frac{\partial}{\partial \hat{t}}T_i = \hat{\chi}^{ITG}\frac{\partial^2}{\partial \hat{r}^2}T_i + \hat{S} + \hat{\chi}_c\frac{\partial^2}{\partial \hat{r}^2}T_i + \hat{\chi}^{NC}\frac{\partial^2}{\partial \hat{r}^2}T_i. \quad (55)$$

These equations are used for transport analysis in the next section. For convenience, ∧ which indicates the normalized variable is omitted hereafter.

3.2 Numerical Analysis

3.2.1 Standard Simulations

Using the extended transport model derived in the previous section, we perform transport simulation and analyze the results. The tri-diagonal matrix in transport equations is solved by recurrence formula, which is discussed appendix A. As initial profiles of ion temperature and density (Fig. 7 and Fig. 8), we use $T_i = T_{i0}(1-r^2)^2$ and $n_i = n_{i0}(1-r^2)$. The heating source is assumed Gaussian distribution, that is, $S = S_0\exp(-(r-r_s)^2/\sigma^2)$ with $r_s = 0.35$ and $\sigma = 0.25$ (Fig. 9). The safety factor is assumed to be given by $q = 1 + 3r^2$ (Fig. 10). The boundary condition are assumed as $U_p = 0$, $\frac{\partial T_i}{\partial r} = 0$ at the center of plasma, and $\frac{\partial^2 U_p}{\partial r^2} = 0$, $T_i = 0$ at the edge. Figure 11 shows the time evolution of heat flux calculated by $q = -(\chi^{ITG} + \chi_c + \chi^{NC})\partial T/\partial r$. It is found that the heat flux evolves diffusively.

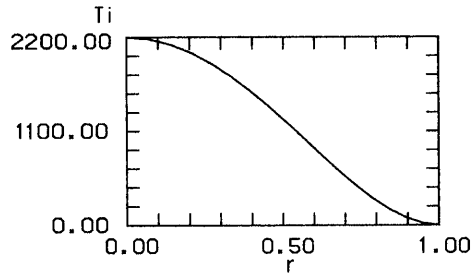

Fig. 7 The radial profile of initial ion temperature; $T_i = T_{i0}(1-r^2)^2$, with $T_{i0} = 2200[eV]$.

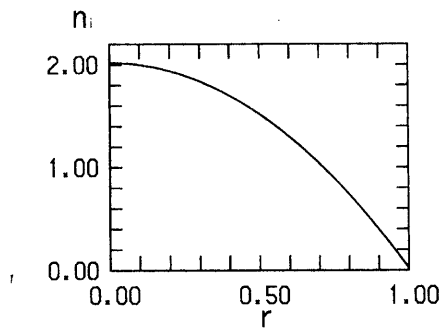

Fig. 8 The radial profile of initial ion density n_i; $n_i = n_{i0}(1-r^2)$ with $n_{i0} = 2[1/(10^{20}m^3)]$.

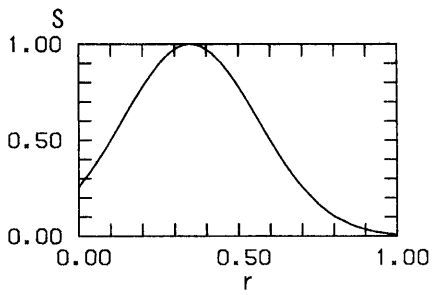

Fig. 9 The radial profile of heating source S which is assumed to be Gussian; $S = S_0 \exp(-(r - r_s)^2/\sigma^2)$, with $r_s = 0.35$ and $\sigma = 0.25$.

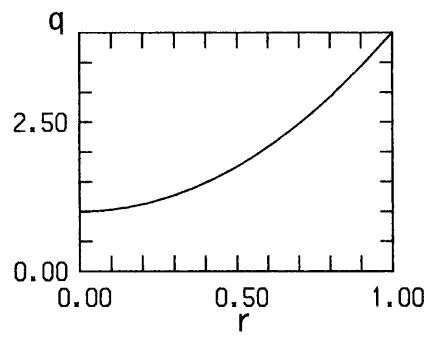

Fig. 10 The radial profile of initial safety factor q; which is assumed $q = -1 + 3r^2$

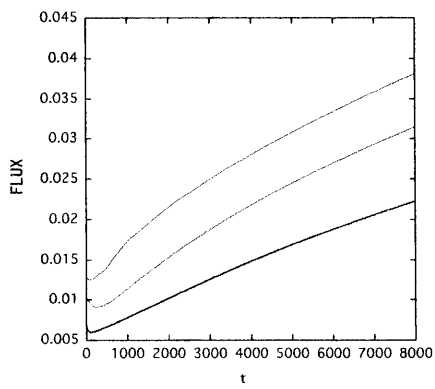

Fig. 11 The time evolution of heat flux at the plasma edge. The black line indicates the flux at $r = 0.95$, the red line, the one at $r = 0.90$, the blue line, the one at $r = 0.85$.

3.2.2 Self-excited Oscillation due to Edge Perturbations

Next, we initially add temperature perturbation. According to the boundary condition at the edge, the

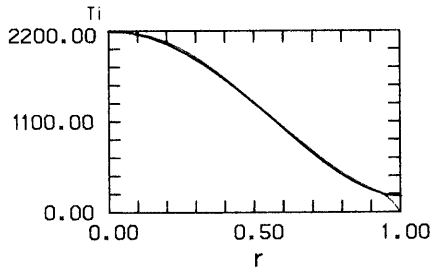

Fig. 12 The black line indicates the radial profile of initial ion temperature at $t = 0$, and the red line, the one at the time with one time step advanced.

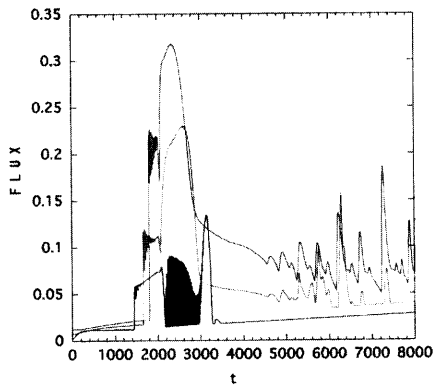

Fig. 13 Time evolution of heat flux. The black line indicates the flux at $r = 0.95$, the red line at $r = 0.90$, the blue line at $r = 0.85$.

temperature is forced to be zero instantenously, which introduces disturbance. In this case, the initial temperature is given by

$$T_i = T_{i0}(1 - r^2)^2 + T_{i1}, \tag{56}$$

with $T_{i0} = 2000[eV]$ and $T_{i1} = 200[eV]$. The initial and the disturbed temperature profiles are shown in Fig. 12. Time evolution of heat flux is shown in Fig. 13. Intermittent behavior is observed which does not appear in the case without disturbance. The flux starts to oscillate periodically with a high frequency on $r = 0.95$ at $t = 2200$. The oscillation with a low frequency occurs on $r = 0.90$ and $r = 0.85$ at $t = 4500$. These oscillations are induced by initial disturbance. We will investigate the mechanism of oscillation in the next subsection.

Analysis of the Observed Oscillation

Figure 14 shows the radial profile of thermal diffusivity χ^{ITG} at $t = 2300$. The solid line represents the thermal diffusivity χ^{ITG} with the E×B shearing rate.

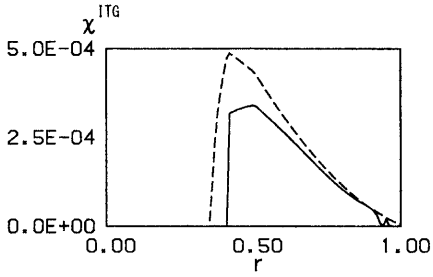

Fig. 14 Radial profile of thermal diffusivity χ^{ITG} at $t = 2300$. The solid line represents in case with E×B shearing rate, the dash line the case without it.

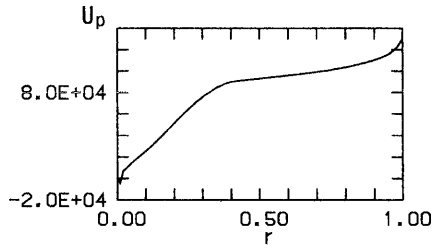

Fig. 15 Radial profile of poloidal flow U_p at $t = 2300$.

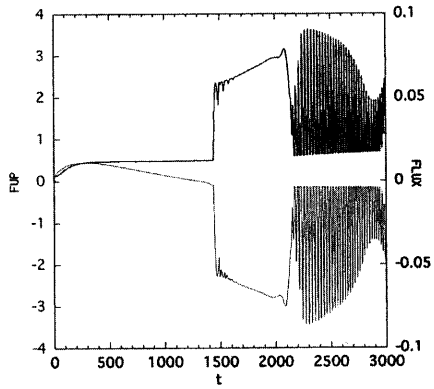

Fig. 16 The red line indicates time evolution of poloidal flow U_p at the point $r = 0.95$. The oscillation is appeared synchronized with the heat flux (the black line).

For the reference, the thermal diffusivity without the E×B shearing rate is also plotted by the dashed line. Figure 15 shows the radial profile of the poloidal flow U_p at $t = 2300$. The χ^{ITG} have a small peak at $r = 0.96$ which implies ITG is unstable at the plasma edge, al-

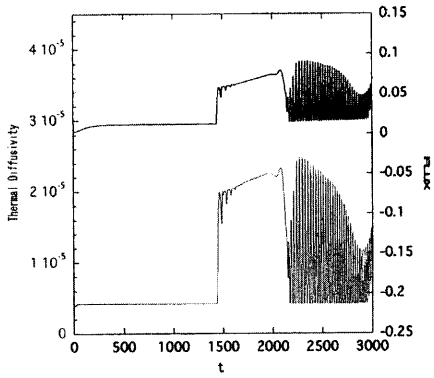

Fig. 17 The red line indicates time evolution of thermal diffusivity χ^{ITG} at the point $r = 0.95$. The oscillation is appeared synchronized with the heat flux (the black line).

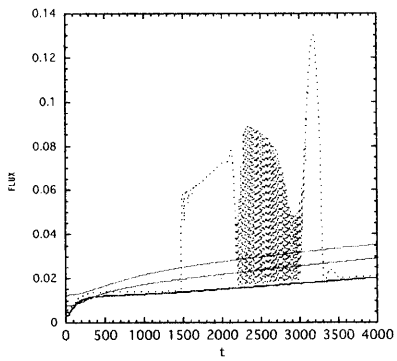

Fig. 18 The time evolution of the heat flux without the poloidal momentum source. The black line indicates the flux at $r = 0.95$, the red line at $r = 0.90$, the blue line at $r = 0.85$. The dash line indicates the result with it.

though the absolute value is very small. It is found that the absolute value of dU_p/dr which corresponds the radial electric field shear is small at the plasma edge as is shown in Fig. 15. This means that the radial electric field shear is not large enough to suppress the ITG mode in the edge region.

Figure 16 shows the time evolution of heat flux and poloidal flow at $r = 0.95$. The black line represents the heat flux and the red line the poloidal flow. It is seen that the heat flux is synchronized with the poloidal flow evolution.

Figure 17 shows the time evolution of the heat flux and the thermal diffusivity. The black line corresponds to the heat flux and the red line to the thermal diffusiv-

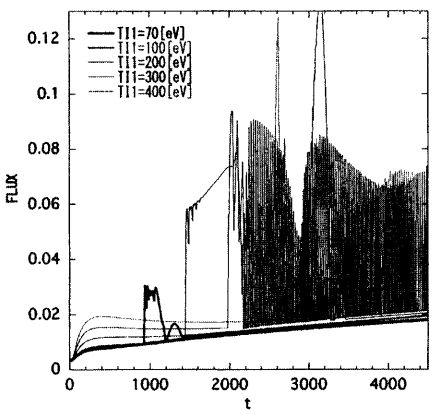

Fig. 19 The time evolution of heat flux with different perturbation amplitude. Five cases are investigated; (1)$T_{i1} = 70[eV]$ (black), (2)$T_{i1} = 100[eV]$ (red), (3)$T_{i1} = 200[eV]$ (green), (4)$T_{i1} = 300[eV]$ (light blue), (5)$T_{i1} = 400[eV]$ (purple).

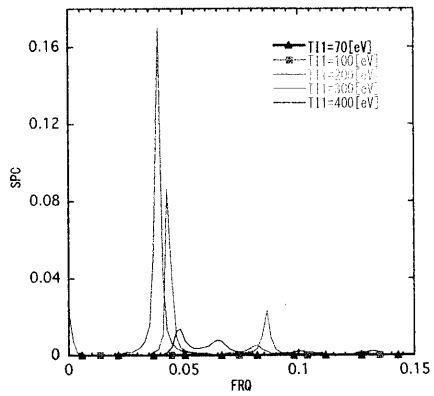

Fig. 20 The frequency stectrum of oscillation of flux at $r = 0.95$ for different perturbation amplitude; (1)$T_{i1} = 70[eV]$ (black), (2)$T_{i1} = 100[eV]$ (red), (3)$T_{i1} = 200[eV]$ (green), (4)$T_{i1} = 300[eV]$ (light blue), (5)$T_{i1} = 400[eV]$ (purple).

ity. These are also synchronized with each other except the fact that the baseline of the heat flux is gradually increasing due to the factor dT_i/dr. The effect of poloidal momentum source is also investigated.

Figure 18 shows the time evolution of the heat flux without the poloidal momentum source. In this case, no oscillation is observed even though the disturbance is given in the egde region. It is concluded that the oscillation occurs due to the destabilization of ITG mode at the edge region. There are two ingredients; i.e., the poloidal momentum source and initial disturbance. If one of them does not exist, the oscillation is not observed. The threshold value for ITG mode might be near the marginal at the edge region, therefore, limit cycle may appear.

Amplitude of Disturbance

We investigated the dependence of the perturbation amplitude on the onset of oscillation. Five cases are investigated; (1)$T_{i1} = 70[eV]$ (black), (2)$T_{i1} = 100[eV]$ (red), (3)$T_{i1} = 200[eV]$ (green), (4)$T_{i1} = 300[eV]$ (light blue), (5)$T_{i1} = 400[eV]$ (purple). Figure 19 shows the time evolution of heat flux for different perturbation amplitude. It is found that oscillation occurs above $T_{i1} = 100[eV]$, but it disappears for $T_{i1} = 70[eV]$. There is the onset threshold located in between $70 - 100[eV]$ in this model.

Spectral Analysis of Oscillation

The spectral analysis of edge oscillation of flux at $r = 0.95$ is performed for different perturbation amplitude. The maximum entropy method is employed to analyze oscillations (See Appendix B). The time sampling of data starts at the time when the periodical oscillation starts in Fig. 19. Figure 20 shows the frequency spectrum of oscillation of flux for different perturbation amplitude; (1)$T_{i1} = 70[eV]$ (black), (2)$T_{i1} = 100[eV]$ (red), (3)$T_{i1} = 200[eV]$ (green), (4)$T_{i1} = 300[eV]$ (light blue), (5)$T_{i1} = 400[eV]$ (purple). It is found that with increasing the amplitude of perturbation, the frequency becomes higher and the amplitude of power spectrum becomes smaller.

3.2.3 Model Dependence of the Self-oscillation

In order to check the model dependence of the self-oscillation, we investigate; (1) alternative model of sharing rate, (2) smoothness of threshold function, (3) mesh numbers, (4) unequally-spaced mesh.

Alternative Model of Sharing Rate

Model dependence on the self-oscillation is investigated. We introduce the alternative model of shearing rate according to Refs. [9, 10] as

$$\hat{\chi}^{ITG} = \frac{\gamma^{ITG} - \gamma_{E\times B}}{k_\perp^2 a v_{Tio}},$$

where

$$\gamma_{E\times B} = \left| \frac{r}{q}\frac{\partial}{\partial r}\frac{q}{r}\frac{cE_r}{B_0} \right|, \tag{57}$$

and

$$\frac{cE_r}{B_0} = -U_p + \frac{e}{\Omega_i m_i a}\frac{\partial}{\partial \hat{r}}\frac{T_i}{e} + \frac{e}{\Omega_i m_i a}\frac{T_i}{e}\frac{1}{n}\frac{dn}{d\hat{r}}. \tag{58}$$

The simulation result by using this model is shown in Fig.21. Interminttency and oscillation is observed at $t =$

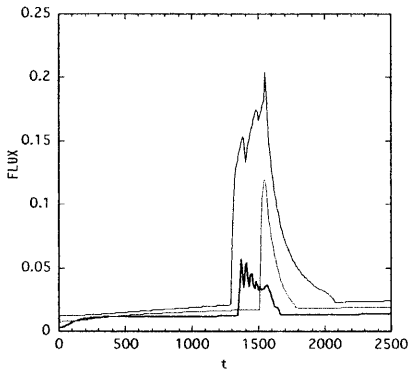

Fig. 21 Time evolution of flux in the case with the alternative model of E×B shearing rate in Ref. [9]. The black line indicates the flux at $r = 0.95$, the red line at $r = 0.90$, the blue line at $r = 0.85$.

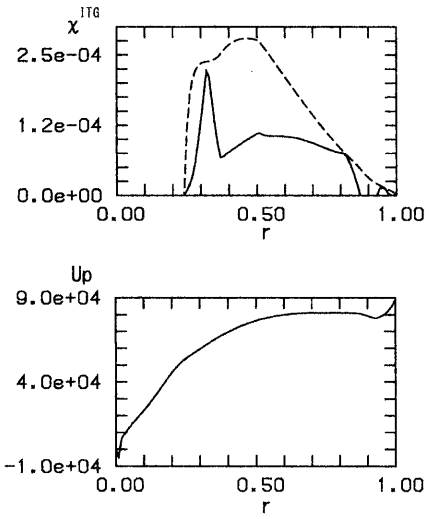

Fig. 22 The radial profiles of χ^{ITG} and U_p at $t = 1400$ with the alternative model of E×B shearing rate in Ref. [9]. (The solid line represents in the case with E×B shearing rate, the dash line does in the case without it.)

1400. However, is stops within a short period. Figure 22 shows the radial profiles of the thermal diffusivity χ^{ITG} and the poloidal flow U_p at $t = 1400$, in the case with edge perturbation. ITG is unstable in the edge region similar to the case in Figs. 14. However, the electric field shear in the edge region is stronger than that in the standard model of shearing rate which is applied in the subsection 3.2.2, so that the oscillation is suppressed at $t \geq 2000$.

Effect of Smoothness of Threshold Function on the Oscillation

We examined the influence of smoothness of threshold function on the oscillation. The function $g(\eta_i) =$

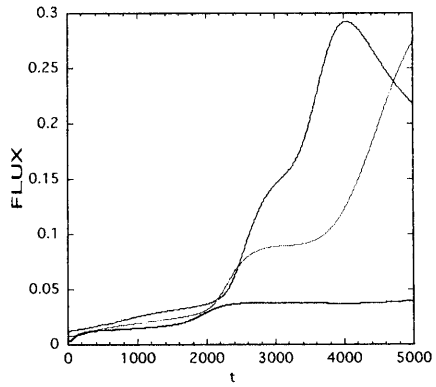

Fig. 23 Time evolution of the heat flux in the case with smoothing threshold function in χ^{ITG}. The black line indicates the flux at $r = 0.95$, the red at $r = 0.90$, the blue at $r = 0.85$.

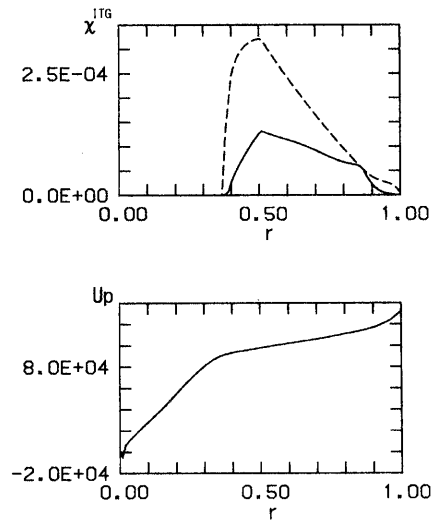

Fig. 24 The radial profiles of χ^{ITG} and U_p at $t = 4000$ in the case with smoothing threshold functions. (The solid line represents in the case with E×B shearing rate, the dash line does in the case without it.)

$\sqrt{\eta_i - \eta_{ic}}$ is interpolated by

$$g(\eta_i) = \begin{cases} 0 & \eta_i \leq \eta_{ic} \\ \mathrm{A}_1(\eta_i - \eta_1)^2 & \eta_1 \leq \eta_i \leq \eta_{ic} \\ \mathrm{A}_2(\eta_i - \eta_{ic}) + \mathrm{A}_3 & \eta_{ic} \leq \eta_i \leq \eta_2 \\ (\eta_i - \eta_{ic})^{0.5} & \eta_2 \leq \eta_i \end{cases} \tag{59}$$

and also χ^{ITG} is interpolated by Pade approximation;

$$\chi^{ITG} = \frac{\gamma^{ITG}}{k_\perp^2 a v_{Ti}} \frac{1}{1 + \gamma_{E\times B}/\gamma^{ITG}}. \tag{60}$$

In this case, it is found that the heat flux evolves diffusively even though the initial perturbation is applied, as shown in Fig. 23. Figure 24 shows the radial profiles of χ^{ITG} and U_p are shown at $t = 4000$. The smoothness of threshold function makes ITG stable in the edge region, so that the oscillation disappears even though the electric field shear itself is small.

Dependence of the Mesh Numbers

We investigate the dependence of the oscillation on the number of mesh points. In the standard calculations, we use $IR_{max} = 100$ grid points in the radial directions and obtain the oscillation if we apply initial perturbation (Fig. 19). Next, we increase the mesh numbers as $IR_{max} = 200$ and investigate the evolution. Figure 25 shows the time evolution of heat flux with $IR_{max} = 200$. The black curve indicates the flux at $r = 0.95$, the red one does it at $r = 0.90$ and the clue one does it at $r = 0.85$. For comparison, the case with $IR_{max} = 100$ at $r = 0.95$ is shown by the dotted curve. It is found that the oscillation disappears in this case. It is because the magnitude of the electric field shear is too large in the edge region so that ITG is completely stabilized as is seen in Fig. 26. The dependence of resolution

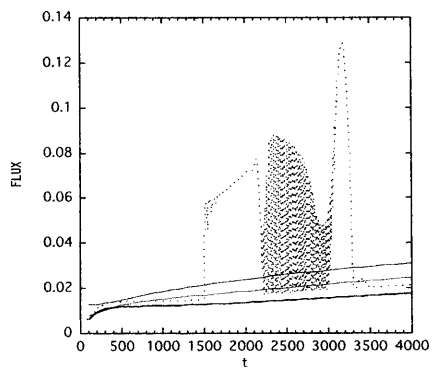

Fig. 25 Time evolution of heat flux in the case with $IR_{max} = 200$. The black curve indicates the flux at $r = 0.95$, the red one at $r = 0.90$ and the blue one at $r = 0.85$. For comparison, the case with $IR_{max} = 100$ at $r = 0.95$ is shown by the dotted curve.

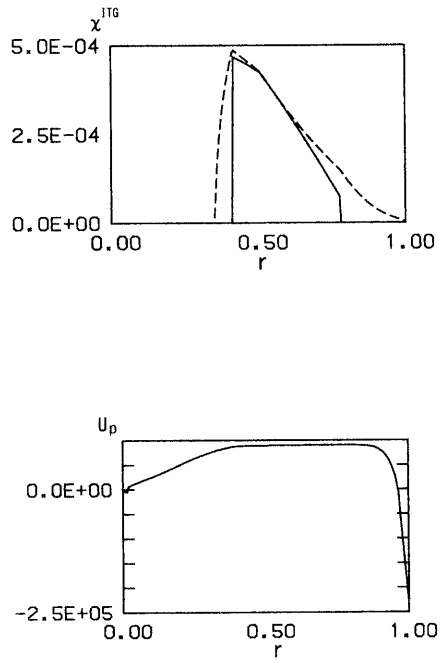

Fig. 26 The radial profiles of χ^{ITG} and U_p at $t = 2000$ in the case with $IR_{max} = 200$. The solid line represents the case with E×B shearing rate, and the dash line, the one without it.

of radial mesh on oscillation should be investigated in detail and be clarified in future work. The simple consideration is made in the next subsection.

Unequally-spaced Mesh

In order to investigate the dependence of the oscillation on the number of mesh points in detail, we introduce an unequally-spaced mesh which accumulates the mesh in the edge region (appendix C). Figure 27 shows the time evolution of heat flux in the case with unequally-spaced mesh. Figure 28 shows the radial profiles of thermal diffusivity and poloidal flow (extended view) at $t = 3000$. It is found that the oscillation also disappears in this case and the radial profile of the diffusivity is the same as the one with regular mesh $IR_{max} = 200$. However, the radial profile of poloidal behavior flow shows the different behavior in the edge region. It is concluded that edge boundary condition and resolution strongly affect on the stability of ITG mode in the edge region through the strength of radial electric shear and also smoothness of threshold function is important facto to produce the oscillations. These elements are not included in 0-D model.

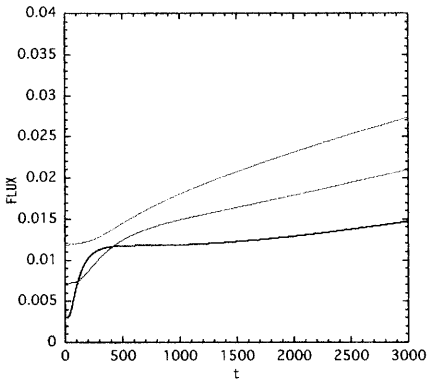

Fig. 27 Time evolution of the heat flux in case with unequally-spaced mesh. The black line indicates the flux at $r = 0.95$, the red line, the one at $r = 0.90$, the blue line, the one at $r = 0.85$.

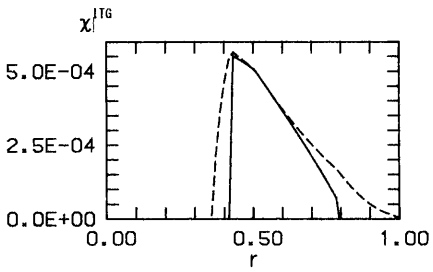

Fig. 28 The radial profile of thermal diffusivity χ_{ITG} calculated by unequally-spaced mesh at $t = 3000$.

4. Summary and Discussion

To investigate the influence of fluctuation for transition and transport, we derived the extended transport models based on MHD ordering not transport ordering. This model includes not only non-ambipolar loss flux [8] but also turbulent diffusivity due to ITG turbulence with E×B shearing rate [11]. Using this model, transport simulations are performed. It is found that the standard model gives the diffusive time evolution of temperature and poloidal flow. To examine the transport response of the system, we introduce the edge perturbation as the initial condition, then trace the time evolution. It is found that if the initial perturbation at the edge exceeds a certain threshold value $T_{i1} \simeq 70$, a periodic oscillation of heat flux occurs. The oscillation is generated by the competition between the destabilization of ITG mode due to the initial perturbation and the stabilization of E×B shearing rate. If the E×B shearing

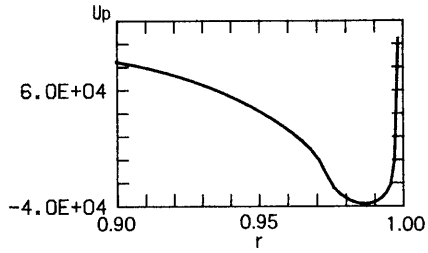

Fig. 29 The extended view of the radial profile of poloidal flow U_p calculated by unequally-spaced mesh at $t = 3000$.

rate is large enough at the edge, the oscillation stops. We also investigate the frequency spectrum of these oscillations. When the initial perturbation increases, the frequency becomes higher and the amplitude of power spectrum becomes smaller. In these simulations ITG mode is found to be near the marginal the edge region and very sensitive to the amplitude of E×B shearing rate.

We then investigate the model dependence and the effect of smoothness of threshold function on the oscillation. It is found that (1) the alternative model of E×B shearing rate by Hahm-Barrel gives the strong stabilization effect on ITG mode in the edge, therefore the oscillation stops in the short period, (2) the smoothness of threshold function is an another ingredient of oscillation and no oscillation occurs in this case large perturbation and even with original E×B sharing rate. Since the E×B shear in the edge region also depends on the resolution of spacial scale, we check the dependence of the oscillation on the number of mesh points. It is found that no oscillation occurs in the case with $IR_{max} = 200$.

The difference between our model and Ref. [3] is that (1) Ref. [3] employes the idealized model with S-curves for non-ambipolor loss flux, but our realistic model does not have so sharp dependence, (2) the boundary condition is also different from each other; Reference [3] uses the free boundary condition, but our boundary condition is the fixed boundary condition which is usually employed in the transport model without scrape-off layer (SOL). In any case, we need improve our model, especially to change the free boundary condition including SOL, This is left as a future work.

Acknowledgment

The author would like to thank Prof. S. -I. Itoh for her guidance, support and continuous encouragement during the course of research, and Dr. M. Yagi for

useful comments, suggestions and help with respect to the computer simulations. She also acknowledge Prof. M.Azumi, Prof. F. Spineanu, Prof. M. Vlad, Prof. P. Diamond and Dr. S. Toda for creative comments. This work is partially supported by collaboration program of Research Institute for Applied Mechanics Kyushu University, and the Grant-in-Aid for Scientific Research of MEXT of Japan.

Furthermore, the author is grateful to her colleague; Mr. Y. Ando, Ms. E. Mori and all classmates in Advanced Energy Engineering Science. She enjoyed her school life with them for two years.

Finally, the author thanks her family for their supports.

References

1) S. -I. Itoh, K. Itoh, Phys. Rev. Lett. 60 (1988) 2276

2) K. C. Shaing and E. C. Crume, Phys. Rev. Lett. 63 (1989) 2369.

3) S. -I. Itoh, K. Itoh and A. Fukuyama, Nucl. Fusion 33 (1993) 1445.

4) S. -I. Itoh, K. Itoh and S. Toda, Plasma Phys. Control. Fusion 45 (2003) 823.

5) S. Toda, S.-I. Itoh, M. Yagi, K. Itoh and A. Fukuyama, J. Phys. Soc. Jpn. 68 (1999) 3520.

6) S. -I. Itoh, K. Itoh, A. Fukuyama, Y. Miura and JFT-2M group Phys. Rev. Lett. 67 (1991) 2485.

7) F. L. Hinton, R. D. Hazeltine, Rev. Mod. Phys. Vol. 48 No. 2 Part1 (1976) 239.

8) F. Romanelli, Phys. Fluids B 1 (1989)1018.

9) T. S. Hahm and K. H. Burrel, Phys. Plasmas 2 (1995) 1648.

10) C. Bouedelle, C. Bourdelle, X. Garbet, G.T. Hoang, J. Ongena and R.V. Budny, Nucl. Fusion 42 (2002) 892.

11) D. E. Newman, B. A. Carreras, D. Lopez-Bruna, P. H. Diamond and V. B. Ledebev, Phys. Plasmas 5 (1998) 938.

Appendix

(A)Recurrence Formula

tri-diagonal system

$$\mathrm{A_i x_{i-1} + B_i x_i + C_i x_{i+1} = D_i}, \ (\mathrm{i} = 1, \cdots, \mathrm{N}-1), \quad (61)$$

where

$$x_i = \mathrm{E_{i-1} x_{i-1} + F_{i-1}}, \quad (62)$$

$$\mathrm{E_i} = -\frac{\mathrm{A_{i+1}}}{\mathrm{B_{i+1} + C_{i+1} E_{i+1}}}, \quad (63)$$

and

$$\mathrm{F_i} = -\frac{\mathrm{D_{i+1} - C_{i+1} F_{i+1}}}{\mathrm{B_{i+1} + C_{i+1} E_{i+1}}}. \quad (64)$$

In the case that x_0, and x_N are given, we obtain

$$\mathrm{E_i} = -\frac{\mathrm{A_{i+1}}}{\mathrm{B_{i+1} + C_{i+1} E_{i+1}}}, \ (\mathrm{i} = \mathrm{N}-2, \cdots, 0), \quad (65)$$

$$\mathrm{F_i} = -\frac{\mathrm{D_{i+1} - C_{i+1} F_{i+1}}}{\mathrm{B_{i+1} + C_{i+1} E_{i+1}}}, \ (\mathrm{i} = \mathrm{N}-2, \cdots, 0), \quad (66)$$

and

$$x_i = \mathrm{E_{i-1} x_{i-1} + F_{i-1}}, \ (\mathrm{i} = 1, \cdots, \mathrm{N}-1). \quad (67)$$

In the case that dx_0/dr, and dx_N/dr are given, we set

$$\left(\frac{\partial x}{\partial r}\right)_j = k_1 x_j + k_2 x_{j+1} + k_3 x_{j+2}, \quad (68)$$

where $x_{j+1} = \mathrm{X}(\mathrm{r_j} + \Delta \mathrm{r})$. Expanding RHS around r_j, we have

$$\left(\frac{\partial x}{\partial r}\right)_j = (k_1 + k_2 + k_3) x_j + (k_2 \Delta r + 2k_3 \Delta r)\left(\frac{\partial x}{\partial r}\right)_j + \left(\frac{k_2 (\Delta r)^2}{2} + \frac{k_3 (2\Delta r)^2}{2}\right)\left(\frac{\partial^2 x}{\partial r^2}\right)_j. \quad (69)$$

Then, the relations should be hold:

$$k_1 + k_2 + k_3 = 0, \qquad k_2 \Delta r + 2k_3 \Delta r = 1,$$
$$\frac{k_2}{2}(\Delta r)^2 + \frac{k_3}{2}(2\Delta r)^2 = 0. \quad (70)$$

Solving these algebraic equations, we obtain the relation:

$$\left(\frac{\partial x}{\partial r}\right)_j = -\frac{3}{2\Delta r} x_j + \frac{2}{\Delta r} x_{j+1} - \frac{1}{2\Delta r} x_{j+2}. \quad (71)$$

Similarly, we have the relation:

$$\left(\frac{\partial x}{\partial r}\right)_j = -\frac{3}{2}\frac{1}{\Delta r} x_j + \frac{2}{\Delta r} x_{j+1} + \frac{1}{2\Delta r} x_{j-2}. \quad (72)$$

where the truncation error is $-\Delta r^2 x^{(3)}/3$.
For the second derivative, the relations are given as

$$\left(\frac{\partial^2 x}{\partial r^2}\right)_j = \frac{2}{\Delta r^2} x_j - \frac{5}{\Delta r^2} x_{j+1} + \frac{4}{\Delta r^2} x_{j+2} - \frac{1}{\Delta r^2} x_{j+3}, \quad (73)$$

and

$$\left(\frac{\partial^2 x}{\partial r^2}\right)_j = -\frac{2}{\Delta r^2} x_j - \frac{5}{\Delta r^2} x_{j-1} + \frac{4}{\Delta r^2} x_{j-2} - \frac{1}{\Delta r^2} x_{j-3}, \quad (74)$$

where the trunction error is $-(11/12)\Delta r^2 x_j^{(3)}/3$.
When $dx_0/dr = \mathrm{A}$, it gives

$$3x_0 - 4x_1 + x_2 = -2\Delta r \mathrm{A} \quad (75)$$

Using $x_1 = \mathrm{E_0x_0 + F_0}$,and $x_2 = \mathrm{E_1x_1 + F_1}$, we obtain

$$x_0 = -\frac{2\Delta r\mathrm{A}}{3-(4-\mathrm{E_1})\mathrm{E_0}} + \frac{(4-\mathrm{E_1})\mathrm{F_0}-\mathrm{F_1}}{3-(4-\mathrm{E_1})\mathrm{E_0}}. \quad (76)$$

Next, when $dx_N/dr = \mathrm{B}$,it gives

$$3x_N - 4x_{N-1} + x_{N-2} = 2\mathrm{B}\Delta\mathrm{r}. \quad (77)$$

Similarly, we obtain

$$x_N = \frac{4\mathrm{A_{N-1}} + \mathrm{B_{N-1}}}{3\mathrm{A_{N-1}} - \mathrm{C_{N-1}}}x_{N-1} - \frac{D_{N-1} - 2\mathrm{B}\Delta\mathrm{r}\mathrm{A_{N-1}}}{3\mathrm{A_{N-1}} - \mathrm{C_{N-1}}}. \quad (78)$$

The comparison of $x_n = \mathrm{E_{N-1}x_{N-1} + F_{N-1}}$ with the above equation gives the relations:

$$\mathrm{E_{N-1}} = \frac{4\mathrm{A_{N-1}} + \mathrm{B_{N-1}}}{3\mathrm{A_{N-1}} - \mathrm{C_{N-1}}}, \quad (79)$$

and

$$\mathrm{F_{N-1}} = -\frac{\mathrm{D_{N-1}} - 2\mathrm{B}\Delta\mathrm{r}\mathrm{A_{N-1}}}{3\mathrm{A_{N-1}} - \mathrm{C_{N-1}}}. \quad (80)$$

When $d^2x_0/dr^2 = \mathrm{A}$,

$$2x_0 - 5x_1 + 4x_2 - x_3 = \mathrm{A}(\Delta\mathrm{r})^2 \quad (81)$$

Using $x_1 = \mathrm{E_0x_0 + F_0}$, $x_2 = \mathrm{E_1x_1 + F_1}$, and $x_3 = \mathrm{E_2x_2 + F_2}$, we obtain

$$x_0 = [5\mathrm{F_0} - 4(\mathrm{E_0F_0} + \mathrm{F_1}) + (\mathrm{E_1E_2F_0} + \mathrm{E_2F_1} + \mathrm{F_2}) + \mathrm{A}(\Delta\mathrm{r})^2]/\mathrm{R}. \quad (82)$$

where $R = 2 - 5\mathrm{E_0} + 4\mathrm{E_0E_1} - \mathrm{E_0E_1E_2}$.
When $d^2x_N/dr^2 = \mathrm{B}$,

$$\mathrm{E_{N-1}} = [-\mathrm{A_{N-1}}(\mathrm{C_{N-2}} - 5\mathrm{A_{N-2}}) + \mathrm{B_{N-2}}(\mathrm{B_{N-2}} + 4\mathrm{A_{N-2}})]/\mathrm{S}, \quad (83)$$

and

$$\mathrm{F_{N-1}} = [-\mathrm{A_{N-1}}(\mathrm{D_{N-2}} + \mathrm{B}(\Delta\mathrm{r})^2\mathrm{A_{N-2}}) + \mathrm{D_{N-1}}(\mathrm{B_{N-1}} + 4\mathrm{A_{N-2}})]/\mathrm{S}. \quad (84)$$

where $S = 2\mathrm{A_{N-2}A_{N-1}} - \mathrm{C_{N-1}}(\mathrm{B_{N-1}} + 4\mathrm{A_{N-2}})$

(B)Spectral Analysis Method

Maximum Entropy Method

(i) Entropy H;

$$H \propto \int_{-f_N}^{f_N} \log P(f)df, \quad (85)$$

where $P(f)$ is time series spectrum, $f_N(\equiv 1/(2\Delta t))$ is Nyquist frequency .

(ii) Wiener-Khintchine's relation equation is

$$\int_{-f_N}^{f_N} P(f)z^k df = C_k(-m \le k \le m), \quad (86)$$

where $C_k(\equiv C_{k\Delta t})$ is auto-correlation function. Another expression is given by

$$\int_{-f_N}^{f_N} \left[P(f)z^k - \frac{1}{2f_N}C(k\Delta t)\right] df = 0. \quad (87)$$

Then, Wiener-Khintchine's relation Eq.86 gives rise to

$$P(f) = \frac{1}{2f_N}\sum_{k=-m}^{m} C_k z^{-k} \quad (88)$$

where

$$z = \exp(i2\pi f\Delta k) \quad (89)$$

(iii) In order to make entropy maximum under the condition [(ii)], we need introduce Lagrange multiplier λ_k, and do variational calculation.

$$\delta\int_{f_N}^{f_N}\left\{\log P - \sum_{k=-m}^{m}\lambda_k\left[P(f)z^k - \frac{C_k}{2f_N}\right]\right\}df = 0 \quad (90)$$

Consequently,

$$P(f) = -\frac{1}{\sum_{k=-m}^{m}\lambda_k z^k} \quad (91)$$

(iv) As $P(f)$ is positive real function, Eq.(91) must be, by substituting a (strange) coefficient γ_k for λ_k,

$$P(f) = \frac{P_m}{2f_N}\frac{1}{|1+\sum_{k=1}^{m}\gamma_k z^k|^2}, \quad (92)$$

where the coefficient is m point prediction error filter, P_m is an average output from P_m.

$$P_m = E\left[\{x_i - (-\gamma_1 x_{i-1} - \cdots - \gamma_m x_{i-m})\}^2\right] = C_0 + \gamma_1 C_1 + \gamma_2 C_2 + \cdots + \gamma_m C_m \quad (93)$$

(v) Since Eq.(88) is equivalent with Eq.(92), z power coefficients of these equations is equal. And more $C_{-m} = C_m$. Therefore, $(m+1)$ dimension simultaneous equations are derived.

$$\begin{bmatrix} C(0) & C(1) & \cdots & C(m) \\ C(1) & C(0) & \cdots & C(m-1) \\ \vdots & \vdots & & \vdots \\ C(m) & C(m-1) & \cdots & C(0) \end{bmatrix} \times \begin{bmatrix} 1 \\ \gamma_1 \\ \vdots \\ \gamma_m \end{bmatrix} = \begin{bmatrix} P_m \\ 0 \\ \vdots \\ 0 \end{bmatrix} \quad (94)$$

(vi) Unknown quantities in Eq.(94) are

$$\gamma_1, \gamma_2, \cdots, \gamma_m; C_m; P_m, \quad (95)$$

the number of which is $m+2$. However the equations is $m+1$, so it is necessary to add a new assumption. As the assumption, "The average output is assumed minimum, when signal are sent to the prediction error filter forward and backward." is adopted.

(vii) If the coefficient $\gamma_1, \cdots, \gamma_m$ and P_m are found, eq.(92) that is next equation gives the MEM spectrum.

$$P(f) = \frac{P_m \triangle t}{|1 + \sum_{k=1}^{m} \gamma_k e^{i2\pi f k \triangle t}|^2} \quad (96)$$

(C)Unequally-spaced Mesh

$$T(x) = ax^2 + bx + c \quad (97)$$

$$a = \frac{\Delta x_i \Delta T_{i+1} - \Delta x_{i+1} \Delta T_i}{2\Delta x_{i+1} \Delta x_i \Delta x_H}, \quad (98)$$

and

$$a = \frac{\Delta x_{i+1}(x_{i+1} + x_i)\Delta T_i - \Delta x_i (x_{i+1} + x_i)\Delta T_{i+1}}{2\Delta x_{i+1} \Delta x_i \Delta x_H}, \quad (99)$$

where $\Delta x_i = x_i - x_{i-1}$, $\Delta x_H = (\Delta x_{i+1} + \Delta x_i)/2 = (x_{i+1} - x_{i-1})/2$. Since $T_i' = 2ax_i + b, T_i'' = 2a$,

$$T_i' = -\frac{\Delta x_{i+1}}{2\Delta x_i \Delta x_H} T_{i-1} + \frac{\Delta x_{i+1} - \Delta x_i}{\Delta x_i \Delta x_{i+1}} T_i + \frac{\Delta x_i}{2\Delta x_{i+1} \Delta x_H} T_{i+1} \quad (100)$$

$$T_i'' = \frac{1}{\Delta x_i \Delta x_H} T_{i-1} + \frac{2}{\Delta x_{i+1} \Delta x_i} T_i + \frac{1}{\Delta x_{i+1} \Delta x_H} T_{i+1} \quad (101)$$

We use x as a parameter of equally-spaced Mesh, and r as one of unequally-spased Mesh.

$$r = Px + (1 - P)\left(1 - \frac{\tanh(Q(1 - x))}{\tanh Q}\right) \quad (102)$$